

Formation of the Young Massive Cluster R136 triggered by Tidally-driven Colliding H I Flows

Yasuo Fukui^{1, 2}, Kisetsu Tsuge², Hidetoshi Sano^{1, 2}, Kenji Bekki³,
Cameron Yozin³, Kengo Tachihara², Tsuyoshi Inoue²

¹Institute for Advanced Research, Nagoya University, Furo-cho, Chikusa-ku, Nagoya 464-8601, Japan

²Department of Physics, Nagoya University, Furo-cho, Chikusa-ku, Nagoya 464-8601, Japan

³ICRAR, M468, The University of Western Australia, 35 Stirling Highway, Crawley Western Australia 6009, Australia

*E-mail: fukui@phys.nagoya-u.ac.jp, tsuge@phys.nagoya-u.ac.jp

Received (reception date); Accepted (acceptation date)

Abstract

Understanding of massive cluster formation is one of the important issues of astronomy. By analyzing the H I data, we have identified that the two H I velocity components (L- and D-components) are colliding toward the H I Ridge, in the southeastern end of the LMC, which hosts the young massive cluster R136 and ~ 400 O/WR stars (Doran et al. 2013) including the progenitor of SN1987A. The collision is possibly evidenced by bridge features connecting the two H I components and complementary distributions between them. We frame a hypothesis that the collision triggered the formation of R136 and the surrounding high-mass stars as well as the H I & Molecular Ridge. Fujimoto & Noguchi (1990) advocated that the last tidal interaction between the LMC and the SMC about 0.2 Gyr ago induced collision of the L- and D-components. This model is consistent with numerical simulations (Bekki & Chiba 2007b). We suggest that a dense H I partly CO cloud of $10^6 M_{\odot}$, a precursor of R136, was formed at the shock-compressed interface between the colliding L- and D-components. We suggest that part of the low-metallicity gas from the SMC was mixed in the tidal interaction based on the *Planck/IRAS* data of dust optical depth (Planck Collaboration et al. 2014).

Key words: Magellanic Clouds — Stars:formation — ISM:individual objects:R136 — ISM:HII regions

1 Introduction

The formation mechanism of super star clusters (SSCs) is a subject of keen astronomical interest, because their extremely energetic interactions with surrounding material, in the form of UV radiation, stellar winds, and supernova explosions, are influential in driving galaxy evolution. In the Milky Way, we have thirteen SSCs as listed in a review article (Portegies Zwart et al. 2010), while the number of SSCs may increase by a more careful search for clusters in future. The young massive cluster RMC136 (R136), which is responsible for ionizing the largest HII region in the Local group (30 Dor), is estimated to have a mass of $10^5 M_{\odot}$, ten-times larger than SSCs in the Milky Way.

Remarkably, R136 hosts the most massive stars over $200 M_{\odot}$ amongst all the SSCs known to date (Crowther et al. 2010). The surroundings of R136 are also exceptionally active star forming regions involving ~ 400 O/WR stars (Doran et al. 2013) associated with rich neutral hydrogen gas. The gas consists of the H I Ridge, the Molecular Ridge and the CO Arc (Luks & Rohlfs 1992; Fukui et al. 1999), and its distribution is highly asymmetric in the LMC.

It has been discussed that the two galaxies the LMC and SMC are interacting with each other in the past and the interaction is influencing the star formation history. Fujimoto & Noguchi (1990) presented a scenario in which the LMC and

SMC had a close encounter 0.2×10^9 yrs ago, which perturbed the HI gas in the both galaxies and caused the current highly asymmetric HI/CO gas distribution in the LMC disk. These authors suggested that the perturbed gas collided with the LMC disk at $50\text{--}100 \text{ km s}^{-1}$ and triggered formation of R136 and the HI Ridge with the highly asymmetric gas distribution. This scenario is supported by the numerical simulations of the galaxy interaction (e.g., Yozin & Bekki 2014), and is consistent with that the HI consists of two velocity features, the L- and D-components (Luks & Rohlfs 1992; see a typical spectrum in Figure 1a), whereas a detailed observational test of the scenario was not undertaken to date.

The aim of the present paper is to analyse the high-angular resolution The Australia Telescope Compact Array (ATCA) +Parkes HI and The Magellanic Mopra Assessment (MAGMA) CO data in order to provide observational evidence for collision between the L- and D-components and to test a scenario of formation of R136 based on cloud-cloud collision (CCC) models (Furukawa et al. 2009; Ohama et al. 2010; Torii et al. 2011; 2015; 2017; Fukui et al. 2014; 2015; 2016; 2017; Saigo et al. 2017).

2 Observational data and masking

The ATCA +Parkes HI 21 cm data (Kim et al. 2005) are used in this study. The resolution of the combined HI image is $1'.0$. This is 15 times higher resolution than that of Luks & Rohlfs (1992), which showed that the HI distribution consists of the L- and D-components. The rms noise fluctuations of the combined map, determined from the line-free parts of the final data cube, is 15 mJy beam^{-1} . This corresponds to a brightness temperature sensitivity of 2.4 K (1σ), for velocity resolution of 1.649 km s^{-1} .

We used the data of the rotational transition of $^{12}\text{CO}(J=1-0)$ observed with NANTEN 4 m telescope (Fukui et al. 1999; 2008; Kawamura et al. 2009; for a review of molecular clouds in the LMC and SMC see Fukui & Kawamura 2010) for a large scale analysis. The half-power beamwidth is $2'.6$, and the velocity resolution is 0.65 km s^{-1} . We also used the MAGMA $^{12}\text{CO}(J=1-0)$ data (Wong et al. 2011) for a detailed analysis. The spatial resolution is $45''$, and the velocity resolution is 0.53 km s^{-1} .

The archival data set of dust optical depth at 353 GHz, τ_{353} , and dust temperature, T_d obtained by the *Planck* and *IRAS* data (see Planck Collaboration et al. 2014 for detail) are used to make comparisons with the HI data. We also used the data from the Southern H-Alpha Sky Survey Atlas (SHASSA) at 656.3 nm wavelength, the $\text{H}\alpha$ emission line of hydrogen (Gaustad et al. 2001). The angular resolution is about $0'.8$, and the sensitivity level is 2 Rayleigh ($1.2 \times 10^{-17} \text{ erg cm}^{-2} \text{ s}^{-1} \text{ arcsec}^{-2}$) pixel^{-1} .

We masked the data in order to eliminate regions with locally heated components and those with different environment as indicated by their high density, by using the $\text{H}\alpha$ and CO data when we compare τ_{353} and HI; the areas showing CO emission higher than 1 K km s^{-1} (1σ) and the areas showing $\text{H}\alpha$ emission higher than 30 Rayleigh are masked (Fukui et al. 2014; Fukui et al. 2015; Okamoto et al. 2017).

3 Results

Following the method of Luks & Rohlfs (1992) we subtracted the galactic rotation in Figure 1, and reproduced their results with $1'.0$ resolution. Figure 1 shows the new images of the two HI components along with the CO clouds. The main feature of the L-component is located toward the CO Arc and in the east of the Molecular Ridge, while the D-component is extended over the galactic disk. We confirmed that the asymmetric distribution of HI in Figure 1a is caused by adding the L-component.

Figure 2 shows two Dec.-velocity diagrams along the CO Arc and the Molecular Ridge. In Figure 2 we find the two velocity components and the bridge features between them. The intensity of the bridge features at each Dec. is correlated with the CO clouds and with the enhanced HI intensity, suggesting collisional interaction in CCC indicated by numerical simulations (Inoue & Fukui 2013; Takahira et al. 2014; Haworth et al. 2015a; 2015b).

Figure 3 shows an overlay of the L- and D-components in the region including 30 Dor. We see the two components show complementary distribution; in Figure 3a the D-component shows intensity depression toward the dense part of the L-component, and the L-component shows depression toward the dense part of the D-component. There are two places of the complementary distribution in the HI Ridge; one is toward (R.A., Dec.) $\sim (5^{\text{h}}40^{\text{m}}0^{\text{s}} - 5^{\text{h}}54^{\text{m}}0^{\text{s}}, -68^{\circ}30'0'' - -70^{\circ}12'0'')$ and the other (R.A., Dec.) $\sim (5^{\text{h}}38^{\text{m}}0^{\text{s}} - 5^{\text{h}}51^{\text{m}}0^{\text{s}}, -70^{\circ}12'0'' - -71^{\circ}30'0'')$.

We find the complementary distribution between the L- and D-components shows some displacement. This displacement between the two complementary features suggests that the relative motion makes a large angle to the line-of-sight (Fukui et al. 2017). We applied the overlapping function $H(\Delta)$ in pc^2 to calculate the displacement in the complementary distribution which is presented in the Appendix of Fukui et al. (2017) in such a way that the two features coincide spatially after the displacement. Specifically, we derived the projected displacement where the overlapping area of the strong L-component (intensity larger than 1000 K km s^{-1}) and the depression of the D-component (intensity smaller than 550 K km s^{-1}) becomes maximum. In Figure 3b we see two HI clouds in the L-component, the north cloud at (R.A., Dec.) $\sim (5^{\text{h}}38^{\text{m}}0^{\text{s}} - 5^{\text{h}}50^{\text{m}}0^{\text{s}}, -68^{\circ}20'0'' - -69^{\circ}48'0'')$ and the

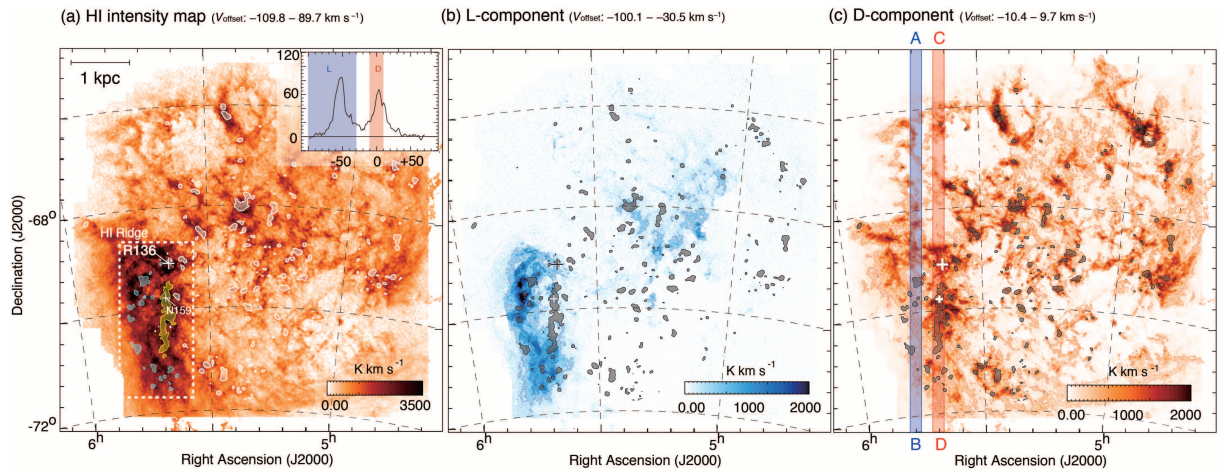


Fig. 1. (a) The HI integrated intensity map with the integration velocity range of $V_{\text{offset}} = -100.1\text{--}89.7 \text{ km s}^{-1}$. The white dashed box illustrate the HI Ridge. The upper right panel shows a typical spectrum of HI at (R.A., Dec.) = ($5^{\text{h}}46^{\text{m}}43^{\text{s}}54, -69^{\circ}42'59''.31$). The horizontal axis and vertical axis indicate V_{offset} [km s $^{-1}$] and intensity [K], respectively. A blue shaded range and a red shaded range indicate the integration velocity range of L- and D-components, respectively. (b) The HI integrated intensity maps of L-component with a velocity range of $-100.1\text{--}30.5 \text{ km s}^{-1}$. The contour levels are 350, 800, 1200, and 2400 K km s $^{-1}$. (c) Same as (b) but for D-component with a velocity range of $-10.4\text{--}9.7 \text{ km s}^{-1}$ and the contour levels of 400, 800, 1200, and 1600 K km s $^{-1}$. The crosses in (b) and (c) denote the positions of R136 and LHA 120-N 159 (N159), while the shaded areas in the 3 panels delineate the regions with CO intensity greater than 3σ with the same velocity range. Those in yellow and blue in (a) indicate the Molecular Ridge and the CO Arc, respectively. The blue and red lines in (c) show the integration ranges in R.A. in Figure 2.

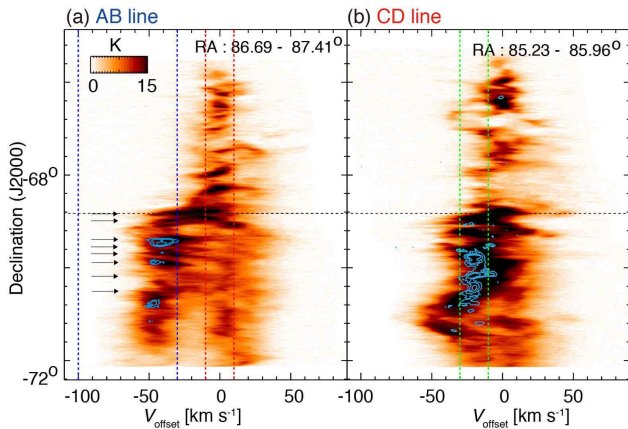


Fig. 2. Dec-velocity diagrams of HI superposed on the CO contour. The position of R136 is indicated by the dashed horizontal line. The contour levels are 0.015, 0.03, and 0.05 K km s $^{-1}$ for each panel. The integration ranges in the R.A. are from $86^{\circ}69'$ to $87^{\circ}41'$ in (a), and $85^{\circ}23'$ to $85^{\circ}96'$ in (b), respectively. The blue and red dashed vertical lines indicate the velocity range of L- and D-components, respectively. The black arrows in (b) indicate the position of bridge features. The green dashed vertical lines indicates intermediate velocity range of L- and D-components.

south cloud at ($5^{\text{h}}36^{\text{m}}0^{\text{s}}\text{--}5^{\text{h}}49^{\text{m}}0^{\text{s}}, -70^{\circ}6'0''\text{--}-71^{\circ}20'0''$), which are surrounded by the D-component. They exhibit a complementary distribution with displacements of 170 pc and 260 pc lengths as shown by the arrows, respectively. We confirmed that the position angle 320 deg. gives the best fit by changing the angle from 315 to 325 deg.

Figure 3c shows a closeup view in the R136 region, showing complementary distributions between the two velocities of HI at

$\sim 100\text{pc}$ scale; the two blue-shifted HI intensity depressions at (R.A., Dec.) = ($5^{\text{h}}40^{\text{m}}0^{\text{s}}\text{--}5^{\text{h}}42^{\text{m}}0^{\text{s}}, -68^{\circ}50'0''\text{--}-69^{\circ}00'0''$) and ($5^{\text{h}}38^{\text{m}}0^{\text{s}}\text{--}5^{\text{h}}42^{\text{m}}0^{\text{s}}, -69^{\circ}04'0''\text{--}-69^{\circ}20'0''$) are clearly associated with the HI components toward the same position, where the HI distribution within 200 pc of R136 is not reliable due to artificial effects of the interferometric fringes.

Figure 4 shows a scatter plot between $W(\text{HI})$ and τ_{353} , where the galactic foreground component is subtracted by using the $W(\text{HI})\text{--}\tau_{353}$ relation (Fukui et al. 2015). The plots for the D-component and the HI Ridge show significantly different slopes by a factor of 2. The difference in the slope corresponds to the difference in metallicity, if we assume that the dust-to-metal ratio is constant in the LMC.

4 Discussion

4.1 Cloud-cloud collision model

The present results indicate that the L- and D-components show observational signatures of cloud-cloud collision, i.e., the two velocity components, the bridge features between them and the complementary distributions. Fukui et al. (2016) summarize and discuss these properties based on observations of ten cases of O star formation, eight in the Milky Way and two in the LMC, and hydrodynamical numerical simulations of cloud-cloud collisions. The differences between the ten previous cases and the present one in the LMC are that the velocity separation 50 km s^{-1} and the size of the colliding components 2 kpc are significantly larger than in the previous cases, and that the O and WR stars including R136 are considerably more numerous than the

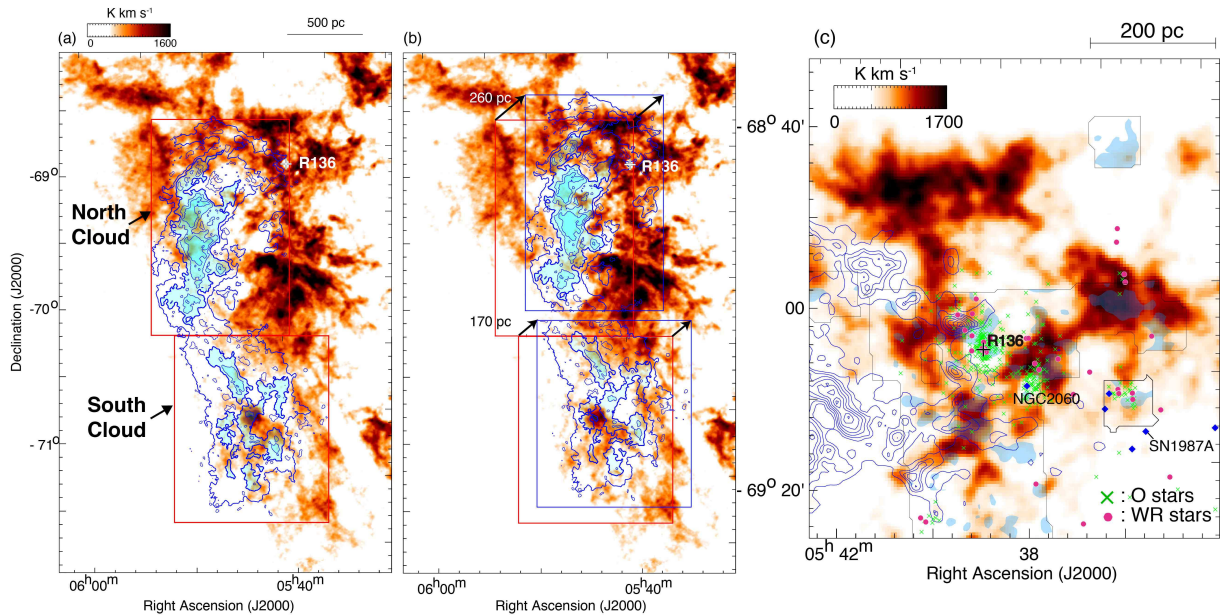


Fig. 3. (a) Hi intensity map of D-component superposed on the L-component's contours of the CO Arc and the Molecular Ridge. The contour levels are 500, 800, 1000, 1200, 1400, 1600, 1800, and 1900 K km s^{-1} . (b) Same image as (a), whereas contours of L-component are displaced. The projected displacements of the northern half and the southern half are 260 pc and 170 pc, respectively, at a position angle of 320 deg. These distances are determined by the overlapping integral function $H(\Delta)$ (see the text and the Appendix of Fukui et al. 2017). The red boxes indicate the initial position of L-component, and the blue boxes of (b) indicate the displaced position. Blue shaded regions of (a) and (b) indicate the Hi intensity is greater than 800 K km s^{-1} . (c) Hi intensity map of D-component superposed on the contours of L-component toward R136. The integration velocity ranges of L- and D-components are the same as Figure 1 and the contour levels are 400, 600, 700, 800, 900, 1100, 1150, 1200, and 1250 K km s^{-1} . The L-component's contours are not displaced. Blue shaded regions indicate the CO intensity of 3σ at the same velocity range with Figure 1(a). Black cross, green crosses, and pink circles indicate the position of R136, O stars, and WR stars respectively. Blue diamonds indicate the positions of SNRs (Maggi et al. 2016).

previous cases (~ 400 in total over an area of $200 \text{ pc} \times 200 \text{ pc}$) (Doran et al. 2013). We see two outstanding stellar condensations in R136 and NGC 2060 (Figure 3c).

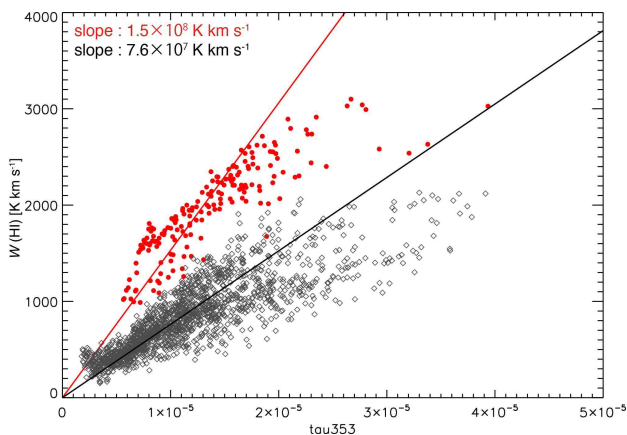


Fig. 4. Scatter plot between τ_{353} and $W(\text{HI})$ for $T_d > 22.5 \text{ K}$. Red points are the data of Arc and Molecular Ridge (the region of Figure 3a), and Grey points are the data of the optical stellar bar region. The red and black linear lines are obtained by the least-squares fit which is assumed to have zero intercept. The data of the direction of the optical stellar bar are used for fitting of the black line, and the red data are used for fitting of the red line.

The major overlapping of the two components in the south-east (Figure 1) is called the Hi Ridge. Hi intensity of Hi Ridge is elevated above a contour level 2000 km s^{-1} . By the optically thin approximation the $N(\text{HI})$ in the ridge is estimated to be $(0.4\text{--}1) \times 10^{22} \text{ cm}^{-2}$ on a 20 pc scale. The Hi Ridge includes two major elongated CO clouds, the Molecular Ridge and the CO Arc. The total mass of the Hi Ridge is estimated to be $1 \times 10^8 M_\odot$ and the molecular masses of the Molecular Ridge and the CO Arc are $1 \times 10^7 M_\odot$ and $0.5 \times 10^7 M_\odot$, respectively (Mizuno et al. 2001). A scenario in which the two velocity Hi components were created by the tidal interaction between the LMC and SMC 2×10^8 yrs ago was presented by Fujimoto & Noguchi (1990). Subsequently, numerical simulations of the galactic interaction and the gas motion were carried out by Bekki & Chiba (2007a) and (2007b). The present analysis shows that the stripped HI gas is at present falling onto the LMC disk at a projected velocity of 50 km s^{-1} , as is consisted with the numerical simulations by Bekki & Chiba (2007b). This interpretation indicates that L-component was on the far side of the LMC disk and is now nearly at the same location with D-component, as suggested by the ongoing collisional interaction.

4.2 Ongoing collision

A possible scenario for the collisional interaction is framed as follows,

1. The region immediately surrounding R136 has a high $N(\text{HI})$ of $\sim 10^{22} \text{ cm}^{-2}$. The other regions of O/WR star formation or O/WR stars are mostly distributed only on the western side of R136, where the parent gas is already strongly dispersed by the stellar ionization. They include the region of the super shell 30 Dor C, the progenitor of SN1987A, etc., which is exposed to us, where we see some CO and HI gas on small scales. The CO gas in the R136 region is strongly dispersed as shown by the recent ALMA results (Indebetouw et al. 2013) whereas it is still associated with massive clumpy HI gas (Figure 2). The age of R136 is estimated to be 1.5 Myrs (Crowther et al. 2016) and the other O/WR stars are probably older than R136 with ages of more than a few Myrs as suggested by the relative paucity of ISM compared with the R136 region. The vicinity of R136 shows an ionized HI cavity of a 15 pc radius (Figure 3c). The formation of the O/WR stars took place some Myrs ago and R136 was most recently formed. By considering the accumulated empirical knowledge (Fukui et al. 2017), we suggest that the distribution of these high mass stars reflects the initial density distribution of the HI gas prior to the collision; very dense compact gas formed R136 by collision and less dense gas formed extended O/WR stars. The masses of the two HI clumps having 100 pc size in Figure 3c are estimated to be $1 \times 10^6 M_{\odot}$. This is consistent with the mass of R136 $1 \times 10^5 M_{\odot}$ which requires a parent cloud of $1 \times 10^6 M_{\odot}$ for an assumed star formation efficiency.
2. The CO Arc region shows two velocity components separated by 50 km s^{-1} , which show clear bridge features as well as complementary distributions typical to collision (Figure 2a). These features indicate that the collision initiated 2 Myrs ago as roughly estimated from a ratio of the cloud size and the velocity $100 \text{ pc}/50 \text{ km s}^{-1}$. The L-component shows a little sign of deceleration, probably because $N(\text{HI})$ of the L-component dominates that of the D-component toward the regions; $N(\text{HI})$ of the L-component is $\sim 4 \times 10^{21} \text{ cm}^{-2}$ while that of the D-component is $\sim 1 \times 10^{21} \text{ cm}^{-2}$. This difference results in little deceleration of the L-component by momentum conservation. The bridge features support the collisional interaction as shown by numerical simulations (Takahira et al. 2014; Haworth et al. 2015b). It is possible that the low average column density in the D-component did not accommodate formation of massive dense clumps in which O stars can form.
3. The Molecular Ridge region shows a single velocity broad feature in Figure 2b with the CO clouds. Their peak velocity lies between L- and D-components after subtraction of the galactic rotation. We suggest that since $N(\text{HI})$ of the two

components was nearly the same, the collision resulted in merging of the two components at their intermediate velocity via momentum conservation. Then, total $N(\text{HI})$ of the merged component was elevated to $\sim 1 \times 10^{22} \text{ cm}^{-2}$. The Molecular Ridge was formed by the strong compression in the collision, while some of the CO gas was formed prior to the collision. In N159 E and W we found collision between filamentary clouds with a velocity of $7\text{--}8 \text{ km s}^{-1}$ by ALMA observations at $1''$ resolution (Fukui et al. 2015; Saigo et al. 2017). It is speculated that the highly filamentary distribution in N159 reflects the gas dynamics in the merging interface layer where filaments are formed according to numerical simulations (Inoue & Fukui 2013).

4.3 GMC/cluster formation

The collision of HI gas flow is able to compress the HI gas and significantly increases the density according to MHD numerical simulations (Inoue & Inutsuka 2012). H_2 clouds are formed in the interface layer in $\sim \text{Myr}$ for density of 10^3 cm^{-3} , and it is expected that the molecular clouds become self-gravitating if they become massive enough. The subsequent process is calculated by Inoue & Fukui (2013) which simulates the colliding flow of dense molecular gas by incorporating self-gravity. These simulations indicate formation of dense clumps which can directly lead to high-mass star formation on smaller scales of 10–20 pc. In a kpc scale collision in the LMC we infer that part of the dense HI gas may be converted into Giant Molecular Clouds (GMCs) if HI gas are decelerated by the collision and further compressed. Fukui et al. (2009) presented a scenario of formation of GMCs in the LMC via gravitational HI accretion by showing the HI becomes denser toward GMCs based on the HI data (Kim et al. 2003).

Figure 4 shows a scatter plot between the dust optical depth at 353 GHz τ_{353} and the 21 cm HI intensity $W(\text{HI})$ in the LMC, where only the highest dust temperature components are shown. We assumed that the highest dust-temperature components ($T_d \lesssim 22.5 \text{ K}$) are most probably optically thin. The overall distribution of the plot is well represented by linear regressions in Figure 4. The points in the HI ridge are shown by red color and show a slope by a factor of 2 steeper than the rest of the points outside the HI Ridge. We interpret that this difference is due to different dust abundance between them; the HI ridge has significantly less dust grains than the rest of the LMC. The numerical simulations by Bekki & Chiba (2007b) shows that the HI gas of the SMC is possibly mixed with the LMC gas in the tidal interaction. If this happens, the HI ridge contains a significant amount of low-metallicity HI of the SMC. The metallicity of the SMC is smaller than that of the LMC by a factor of five (Rolleston et al. 2002). If the HI ridge consists of HI mass both from the SMC and LMC at a ratio of 1:1, for sub-solar met-

ality 1/10 in the SMC and the 1/2 in the LMC, a factor of 2 different slopes in Figure 4 is explained, lending a support for the tidal origin of the HI ridge (Fukui et al. 2014; 2015).

5 Conclusions

We found signatures of a collision over a few kpc between the two velocity HI components toward R136, the HI Ridge including the Molecular Ridge & the CO Arc in the LMC. The blue-shifted HI L-component was created in the galaxy interaction 0.2 Gyrs ago via tidal stripping between the LMC and the SMC. In 0.2 Gyrs, the perturbed HI gas is now colliding interacting with the HI gas in the LMC disk. The collision formed ~ 400 O/WR stars in the HI Ridge which includes R136, N159 and the other active star forming GMCs, alongside the CO Arc, as supported by numerical simulations of colliding HI flows.

Acknowledgments

This work was financially supported in part by JSPS KAKENHI Grant Numbers 16K17664 and 16H05694. This work was also financially supported by Career Development Project for Researchers of Allied Universities. The ATCA, Parkes and Mopra radio telescope are part of the ATNF which is funded by the Australian Government for operation as a National Facility managed by CSIRO. The UNSW Digital Filter Bank used for the observations with the Mopra Telescope was provided with support from the Australian Research Council. Based on observations obtained with Planck, an ESA science mission with instruments and contributions directly funded by ESA Member States, NASA, and Canada. The Southern H-Alpha Sky Survey Atlas, which is supported by the National Science Foundation.

References

- Bekki, K., & Chiba, M. 2007, MNRAS, 381, L16
 Bekki, K., & Chiba, M. 2007, PASA, 24, 21
 Crowther, P. A., Schnurr, O., Hirschi, R., et al. 2010, MNRAS, 408, 731
 Crowther, P. A., Caballero-Nieves, S. M., Bostroem, K. A., et al. 2016, MNRAS, 458, 624
 Doran, E. I., Crowther, P. A., de Koter, A., et al. 2013, A&A, 558, A134
 Fujimoto, M., & Noguchi, M. 1990, PASJ, 42, 505
 Fukui, Y., Mizuno, N., Yamaguchi, R., et al. 1999, PASJ, 51, 745
 Fukui, Y., Kawamura, A., Minamidani, T., et al. 2008, ApJS, 178, 56-70
 Fukui, Y., Kawamura, A., Wong, T., et al. 2009, ApJ, 705, 144
 Fukui, Y., & Kawamura, A. 2010, ARA&A, 48, 547
 Fukui, Y., Ohama, A., Hanaoka, N., et al. 2014, ApJ, 780, 36
 Fukui, Y., Okamoto, R., Kaji, R., et al. 2014, ApJ, 796, 59
 Fukui, Y., Harada, R., Tokuda, K., et al. 2015, ApJL, 807, L4
 Fukui, Y., Torii, K., Onishi, T., et al. 2015, ApJ, 798, 6
 Fukui, Y., Torii, K., Ohama, A., et al. 2016, ApJ, 820, 26
 Fukui, Y., Torii, K., Hattori, Y., et al. 2017, arXiv:1701.04669
 Furukawa, N., Dawson, J. R., Ohama, A., et al. 2009, ApJL, 696, L115
 Gaustad, J. E., McCullough, P. R., Rosing, W., & Van Buren, D. 2001, PASP, 113, 132
 Haworth, T. J., Shima, K., Tasker, E. J., et al. 2015b, MNRAS, 454, 1634
 Haworth, T. J., Tasker, E. J., Fukui, Y., et al. 2015a, MNRAS, 450, 10
 Indebetouw, R., Brogan, C., Chen, C.-H. R., et al. 2013, ApJ, 774, 73
 Inoue, T., & Fukui, Y. 2013, ApJ, 774, L31
 Inoue, T., & Inutsuka, S.-i. 2012, ApJ, 759, 35
 Kawamura, A., Minamidani, T., Mizuno, Y., et al. 2009, Globular Clusters - Guides to Galaxies, 121
 Kim, S., Staveley-Smith, L., Dopita, M. A., et al. 2003, ApJS, 148, 473
 Kim, S., Staveley-Smith, L., Dopita, M. A., et al. 2005, arXiv:astro-ph/0506224
 Luks, T., & Rohlfs, K. 1992, A&A, 263, 41
 Maggi, P., Haberl, F., Kavanagh, P. J., et al. 2016, A&A, 585, A162
 Mizuno, N., Yamaguchi, R., Mizuno, A., et al. 2001, PASJ, 53, 971
 Ohama, A., Dawson, J. R., Furukawa, N., et al. 2010, ApJ, 709, 975
 Okamoto, R., Fukui, Y., et al. 2017, ApJ in press, arXiv:1612.07696v2
 Planck Collaboration, Abergel, A., Ade, P. A. R., et al. 2014, A&A, 571, A11
 Portegies Zwart, S. F., McMillan, S. L. W., & Gieles, M. 2010, ARA&A, 48, 431
 Rolleston, W. R. J., Trundle, C., & Dufton, P. L. 2002, A&A, 396, 53
 Saigo, K., Onishi, T., Nayak, O., et al. 2017, ApJ, 835, 108
 Takahira, K., Tasker, E. J., & Habe, A. 2014, ApJ, 792, 63
 Torii, K., Enokiya, R., Sano, H., et al. 2011, ApJ, 738, 46
 Torii, K., Hasegawa, K., Hattori, Y., et al. 2015, ApJ, 806, 7
 Torii, K., Hattori, Y., Hasegawa, K., et al. 2017, ApJ, 835, 142
 Yozin, C., & Bekki, K. 2014, MNRAS, 443, 522
 Wong, T., Hughes, A., Ott, J., et al. 2011, ApJS, 197, 16